

Diese Arbeit wurde vorgelegt am Aerodynamischen Institut

Large eddy simulation of particle-laden decaying isotropic turbulence using an Euler-Lagrange method

MASTERARBEIT ALLGEMEINER MASCHINENBAU
VON
KONSTANTIN FRÖHLICH

Aerodynamisches Institut der RWTH Aachen

27. September 2016

Betreuer: Dipl.-Ing. Lennart Schneiders
Erstprüfer: Univ.-Prof. Dr.-Ing. Wolfgang Schröder

Contents

Nomenclature	II
1 Introduction	1
2 Mathematical models	4
2.1 Equations governing the carrier flow	4
2.2 The Euler-Lagrange method for particle-laden flows	5
3 Numerical methods	8
3.1 Spatial and temporal discretization of the carrier flow	8
3.2 Turbulence modeling	9
3.3 Solution schemes for the Euler-Lagrange method	11
4 Results and discussion	13
4.1 Simulation of the carrier flow	13
4.1.1 Initial condition and flow configuration	13
4.1.2 Results	15
4.2 Simulation of particle-laden isotropic decaying turbulence	21
5 Conclusion and outlook	26

Nomenclature

Acronyms

ADM	approximate deconvolution method
DNS	direct numerical simulation
LES	large eddy simulation
rms	root-mean square
SGS	subgrid scales

Greek symbols

γ	capacity ratio
δt	time step size
δx	grid spacing
Δ	filter width
ϵ	viscous dissipation rate
ϵ_0	initial viscous dissipation rate
ϵ_ν	resolved part of the viscous dissipation rate ϵ
η_k	Kolmogorov length scale
κ	grid resolution dependent constant to enhance centralization of numerical viscous fluxes
λ	grid resolution dependent constant to enhance centralization of numerical convective fluxes
λ_0	initial Taylor microscale
μ	dynamic viscosity
μ_∞	reference dynamic viscosity
ν	kinematic viscosity
ρ_∞	reference fluid density
ρ_f	fluid density
ρ_p	particle density

$\bar{\tau}$	stress tensor
τ	auxiliary variable for integration over the time
τ_k	Kolmogorov time scale
τ_p	particle response time
τ_{sgs}	smallest resolved time scale
τ_{ij}^{R}	anisotropic part of the SGS stresses
$\hat{\tau}_{ij}$	filtered stress tensor
Φ_p	particle volume fraction
$\phi(\mathbf{x}, t)$	auxiliary vector for the definition of the filtering operation
$\phi'(\mathbf{x}, t)$	fine scale part of $\phi(\mathbf{x}, t)$
$\hat{\phi}(\mathbf{x}, t)$	large scale part of $\phi(\mathbf{x}, t)$
$\phi(Re_p)$	empirical correction function for Stokes drag
$\langle \phi \rangle$	ensemble average of ϕ
ψ_p	particle mass fraction

Roman symbols

A	surface area
a	speed of sound
C_M	added-mass coefficient
c_p	specific heat capacity at constant pressure
C_S	Smagorinsky coefficient
c_v	specific heat capacity at constant volume
d_p	particle diameter
E	total specific energy
e	internal energy
$E(k)$	energy spectrum
$E_{k,0}$	initial turbulent kinetic energy
E_k	turbulent kinetic energy
E_p	average kinetic energy of the particles
\mathbf{F}	coupling force vector
\mathbf{g}	acceleration of gravity vector
$G(\mathbf{x}, \Delta)$	spatial convolution filter

$\bar{\mathbf{H}}$	flux tensor
$\bar{\mathbf{H}}_{\text{inv}}$	inviscid part of the flux tensor
$\bar{\mathbf{H}}_{\text{visc}}$	viscous part of the flux tensor
$\bar{\mathbf{I}}$	unit tensor
$(k/k_0)_{\text{max}}$	maximal resolvable wave number
k	wave number
$K(t, \tau)$	kernel of the Basset history
k_0	base wave number
k_p	peak wave number
k_t	thermal conductivity
L	edge length of a cube
L_∞	reference length
l_0	length scale of the largest eddy
m_f	mass of the fluid
M_1^n	normal Mach number at the left side of a cell surface
m_p	overall mass of particles
M_r^n	normal Mach number at the right side of a cell surface
\mathbf{n}	normal of a control volume in outward direction
\hat{p}	filtered pressure
p	pressure
Pr	Prandtl number
\mathbf{Q}	vector of conservative Eulerian variables
\mathbf{q}	heat conduction vector
R	specific gas constant
Re	Reynolds number
$Re_{\lambda 0}$	initial microscale Reynolds number
Re_p	particle Reynolds number
$\bar{\mathbf{S}}$	rate-of-strain tensor
\hat{S}_{ij}	filtered rate-of-strain tensor
S	Sutherland temperature
S_3	skewness of the velocity derivative

S_{sgs}	subgrid-activity
St	Stokes number
T	temperature
T_{∞}	reference temperature
t	time
\mathbf{u}'	rms-velocity vector
\mathbf{u}	fluid velocity vector
\hat{u}_i	filtered velocity component in i th direction
u_0	initial dimensionless rms-velocity
u_{∞}	reference fluid velocity
$u_{i+1/2}$	velocity component at the cell surface between the i th and the $(i+1)$ th cell
u_i	velocity component at the i th cell
u_L	extrapolated velocity component at the left side of a cell surface
u_L^*	modified extrapolated velocity component at the left side of a cell surface
u_R	extrapolated velocity component at the right side of a cell surface
u_R^*	modified extrapolated velocity component at the right side of a cell surface
\mathbf{v}	particle velocity vector
V	control volume
V_p	overall particle volume
\mathbf{x}_p	particle position vector
\mathbf{x}	coordinate vector
x	auxiliary coordinate for the definition of finite difference expressions
x_i	coordinate in i th direction
\mathbf{y}	auxiliary coordinate vector for spatial integration
z	factor for centralizing the extrapolation of a velocity component onto a cell surface

1 Introduction

Particle-laden turbulent flow is of importance in a broad field of applications including natural and technical environments. Examples may be found in the settling of aerosol particles in atmospheric flows, in the transport of dust through the human respiration system, in fuel injections of internal combustion engines, as well as in the combustion of pulverized coal particles in a furnace. Additionally, the interaction of particles with the turbulent carrier flow is of fundamental research interest. Due to the numerous scales involved, particle-laden flow reveals complex interaction phenomena. For instance, particles tend to collect in regions of high strain rate and low vorticity which results in "preferential concentration" (Squires and Eaton, 1991), i.e. turbulence may suppress the mixing of particles in comparison to quiescent conditions. The actual behavior of particle-laden flows is often characterized by the ratio of the particle response time, τ_p , to the Kolmogorov time scale τ_k . Particles with $\tau_p/\tau_k \ll 1$ and finite inertia follow the carrier flow and enhance its turbulent kinetic energy since they maintain their kinetic energy longer than the carrier flow. Whereas particles with a $\tau_p/\tau_k > 1$ reduce the turbulent kinetic energy because of the "crossing trajectories" effect (Ferrante and Elghobashi, 2003). The presence of gravity further extends the complexity. An initially isotropic flow becomes anisotropic in the large scales due to anisotropic inertia exchange between the particles and the carrier flow at small scales (Elghobashi and Truesdell, 1993). Additionally, an increased average settling velocity of particles may be observed in turbulent flows. Wang and Maxey (1993) identified the effect of "preferential sweeping". Inertial particles travelling along their trajectories tend to move in the downward direction of vortices. That is, particles "see" a downward flow in isotropic turbulent flow due to their volume force pointing in downward direction.

A powerful numerical technique for the analysis of particle-laden flows is the direct numerical simulation (DNS). However, DNS requires extensive usage of computational resources even for the simplest cases, which motivates the use of large eddy simulation (LES). LES resolves large energy-containing scales while using models for small subgrid scales (SGS) mainly responsible for the dissipation. Since

the interaction of particles with the carrier flow often happens at the SGS, LES of particle-laden flows is a present subject of research. For instance, in LES of pulverized coal combustion, the influence of SGS on the particles is either neglected (Apte et al., 2003) or approximated using a stochastic model (Bermudez et al., 2011; Franchetti et al., 2013). However, Armenio et al. (1999) pointed out that the accuracy of LES without any particle model is strongly dependent on the grid resolution. It was found that the quality of particle-laden LES depends on the amount of kinetic energy lost by the filtering process. Additionally, Gobert and Manhart (2010) examined different particle models for LES and concluded that stochastic models are insufficient for particles with higher inertia. Hence, the development of an accurate particle model for LES remains unclosed.

This thesis will serve as a first step for the development of new models capable of predicting particle-laden flows using implicit LES. Therefore, a setup is developed which allows a comparison between the results of LES and DNS of particle-laden flows by controlling the numerical dissipation introduced by second-order solution schemes. Subsequently, the setup will be used to identify first effects, which have to be overcome by the models. The case of isothermal, nearly incompressible isotropic decaying turbulence will be analyzed as the carrier flow. The reason for this type of flow is given by the extensive research activity and thus by the availability of reference data. However, homogeneous isotropic turbulence is also a universal case. According to Kolmogorov's hypothesis of local isotropy, the small-scale motions of any flow are isotropic at sufficiently high Reynolds numbers (e.g. Batchelor (1956)). The case of particle-laden isotropic turbulent flow needs to be well understood before moving on with the more complex case of inhomogeneous turbulence. Therefore, the particle-laden flow will be examined in the absence of gravity.

The structure of this thesis is as follows. Chapter 2 proposes the common mathematical models for the carrier flow and a popular Euler-Lagrange model. The conservation equations of mass, momentum and energy of the carrier flow will be presented, followed by a semi-empirical version of the Maxey-Riley equation including common simplifications. In Chapter 3, numerical methods capable of solving the mathematical model equations will be introduced. It will be mainly focused on the capabilities of controlling the dissipation of the numerical schemes, which becomes important for the implicit turbulence modeling in LES. Subsequently, these schemes will be used in Chapter 4. A setup for decaying isotropic turbulence will be introduced and parameters of the numerical schemes adjusted, such that the implicit LES is capable of predicting the particle-free carrier flow

accurately. Chapter 4 will be closed by an analysis of particle-laden LES. The thesis will be concluded by Chapter 5 with a discussion about areas for future development.

2 Mathematical models

In this section, mathematical models are introduced which are capable of describing the motion of small particles suspended in a flow. The mathematical model of the fluid phase will be given in Sec. 2.1. Subsequently, the motion of particles will be described by model equations using a Lagrangian point particle approach in Sec. 2.2.

2.1 Equations governing the carrier flow

The conservation of mass, momentum, and energy in a control volume V may be expressed in integral form by

$$\int_V \frac{\partial \mathbf{Q}}{\partial t} dV + \int_{\partial V} \bar{\mathbf{H}} \cdot \mathbf{n} dA = \mathbf{0}, \quad (2.1)$$

where $\mathbf{Q} = [\rho_f, \rho_f \mathbf{u}, \rho_f E]^T$ is the vector of conservative Eulerian variables and $\bar{\mathbf{H}}$ is the flux tensor through the surface ∂V of V in outward normal direction \mathbf{n} . The conservative variables are defined by the fluid density ρ_f , the vector of velocities \mathbf{u} , and the total specific energy $E = e + |\mathbf{u}|^2/2$ containing the specific internal energy e . It is physically meaningful as well as useful for the development of numerical schemes to divide $\bar{\mathbf{H}}$ into an inviscid part $\bar{\mathbf{H}}_{\text{inv}}$ and a viscous part $\bar{\mathbf{H}}_{\text{visc}}$, where

$$\bar{\mathbf{H}} = \bar{\mathbf{H}}_{\text{inv}} + \bar{\mathbf{H}}_{\text{visc}} = \begin{pmatrix} \rho_f \mathbf{u} \\ \rho_f \mathbf{u} \mathbf{u} + p \\ \mathbf{u} (\rho_f E + p) \end{pmatrix} - \frac{1}{Re} \begin{pmatrix} \mathbf{0} \\ \bar{\boldsymbol{\tau}} \\ \bar{\boldsymbol{\tau}} \mathbf{u} - \mathbf{q} \end{pmatrix}, \quad (2.2)$$

with the pressure p , the stress tensor $\bar{\boldsymbol{\tau}}$, the vector of heat conduction \mathbf{q} , and the Reynolds number Re . The latter is determined by $Re = \frac{\rho_\infty u_\infty L}{\mu_\infty}$, given the reference quantities of the density ρ_∞ , the velocity u_∞ , the length L , and the dynamic viscosity μ_∞ . Using Stokes' hypothesis for a Newtonian fluid yields an equation for the stress tensor

$$\bar{\boldsymbol{\tau}} = 2\mu \bar{\mathbf{S}} - \frac{2}{3}\mu (\nabla \cdot \mathbf{u}) \bar{\mathbf{I}}, \quad (2.3)$$

in which $\bar{\mathbf{I}}$ is the unit tensor and $\bar{\mathbf{S}}$ holds the rate-of-strain tensor defined as $\bar{\mathbf{S}} = \frac{(\nabla \mathbf{u} + (\nabla \mathbf{u})^T)}{2}$. The dynamic viscosity μ depends on the local thermodynamic state of the fluid. However, it can be approximately obtained by Sutherland's law

$$\mu(T) = \mu_\infty \left(\frac{T}{T_\infty} \right)^{3/2} \frac{T_\infty + S}{T + S}, \quad (2.4)$$

with S being the Sutherland temperature. Fourier's law gives the heat conduction

$$\mathbf{q} = -\frac{\mu}{Pr(\gamma - 1)} \nabla T, \quad (2.5)$$

using the static temperature T , the constant capacity ratio $\gamma = c_p/c_v$, the specific heat capacities c_v and c_p at constant volume and at constant pressure. The Prandtl number Pr is given by $Pr = \frac{\mu_\infty c_p}{k_t}$ containing the thermal conductivity k_t . The system of equations can be closed by the caloric state equation $e = c_v T$ and the state equation of an ideal gas $p = \rho R T$, with R being the specific gas constant.

The integral formulation of the conservation equations (2.1) is particularly useful for a finite-volume solution scheme. However, applying Gauss's theorem yields

$$\frac{\partial \mathbf{Q}}{\partial t} + \nabla \cdot \bar{\mathbf{H}} = \mathbf{0}, \quad (2.6)$$

which will be required for the formulation of the filtered equations in Sec. 3.2.

2.2 The Euler-Lagrange method for particle-laden flows

In this thesis, dilute suspensions of small, rigid, spherical particles modeled by point particles without collisions are investigated. The volume fraction $\Phi_p = V_p/V$, with the volume occupied by particles V_p and the overall volume V , is small, i.e. $\Phi_p \ll 1$. The mass fraction $\psi_p = m_p/m_f$, with the overall mass of particles m_p and the mass of the fluid m_f , is kept constant ≈ 1 , which yields an interaction between inertial particles and the smallest turbulent scales referred to as two-way coupling. This interaction is often characterized by the Stokes number $St = \tau_p/\tau_k$ where the particle response time may be obtained by $\tau_p = \frac{(\rho_p/\rho_f)d_p^2}{18\nu}$ using the particle density ρ_p , the particle diameter d_p , and the Kolmogorov time scale, defined as $\tau_k = (\nu/\epsilon)^{1/2}$ with the viscous dissipation rate ϵ and the kinematic viscosity ν . The trajectories of the particles are computed by applying a popular semi-empirical modulation

(e.g. Balachandar and Eaton (2010)) of the Maxey-Riley equation (Maxey and Riley, 1983) which is stated by

$$m_p \frac{d\mathbf{v}}{dt} = 3\pi\mu d_p(\mathbf{u} - \mathbf{v})\phi(Re_p) + m_f \frac{D\mathbf{u}}{Dt} + m_f C_M \left(\frac{D\mathbf{u}}{Dt} - \frac{d\mathbf{v}}{dt} \right) + \frac{3}{2} d_p^2 \sqrt{\pi\rho_f\mu} \int_{-\infty}^t K(t, \tau) \frac{d(\mathbf{u} - \mathbf{v})}{d\tau} d\tau + (m_p - m_f)\mathbf{g}, \quad (2.7)$$

where $\mathbf{u} = \mathbf{u}(\mathbf{x}_p, t)$ is the velocity of the *undisturbed* fluid at the particle position \mathbf{x}_p , $\mathbf{v} = \mathbf{v}(\mathbf{x}_p, t)$ is the particle velocity, and D/Dt denotes the total derivative following the fluid stream lines, whereas d/dt the total derivative following the particle trajectory. The explanations of the individual contributions on the right-hand side of Eq. (2.7) are described in the following:

- $3\pi\mu d_p(\mathbf{u} - \mathbf{v})\phi(Re_p)$:
quasi-steady Stokes drag with an empirical correction function
 $\phi(Re_p) = 1 + 0.15Re_p^{0.687}$ containing the particle Reynolds number Re_p
- $m_f \frac{D\mathbf{u}}{Dt}$:
pressure gradient of the carrier flow
- $m_f C_M \left(\frac{D\mathbf{u}}{Dt} - \frac{d\mathbf{v}}{dt} \right)$:
added-mass term with C_M as added-mass coefficient, i.e. the force which a particle experiences due to the acceleration of the inertial surrounding fluid
- $\frac{3}{2} d_p^2 \sqrt{\pi\rho_f\mu} \int_{-\infty}^t K(t, \tau) \frac{d(\mathbf{u} - \mathbf{v})}{d\tau} d\tau$:
Basset history term with the kernel $K(t, \tau)$ describing the history of relative acceleration
- $(m_p - m_f)\mathbf{g}$:
acceleration due to gravity \mathbf{g}

Maxey and Riley (ibid.) already estimated that for $d_p/\eta_k \ll 1$, with $\eta_k = (\nu^3/\epsilon)^{0.25}$ the Kolmogorov length, and for $Re_p \ll 1$ the unsteady forces may be negligible. While the latter constraint can approximately be overcome by the empirical function $\phi(Re_p)$, $d_p/\eta_k \ll 1$ essentially limits the range of applications of Eq. (2.7). Specifically, with $\eta_k \sim l_0 Re^{-3/4}$ and l_0 as the length scale of the largest eddy (e.g. Pope (2000)), Eq. (2.7) has only restricted significance for industrial and natural flow conditions which have in general a high Re . Indeed, Balachandar and Eaton (2010) pointed out that the development of Lagrangian formulations for large particles $d_p \gtrsim \eta_k$ is a future direction of research, but also that the

Lagrangian approach provides arguably the only option to deal with large particles.

In this thesis, particles with $d_p/\eta_k \ll 1$ are analyzed neglecting the gravity. Thus, Eq. (2.7) may be reduced to

$$\mathbf{F} = m_p \frac{d\mathbf{v}}{dt} = 3\pi\mu d_p(\mathbf{u} - \mathbf{v})\phi(Re_p). \quad (2.8)$$

Elghobashi and Truesdell (1992) performed numerical tests to quantify the differences between Eqs. (2.7) and (2.8) for decaying isotropic turbulence. The result of less than 4% justifies this simplification. Note, that the coupling force \mathbf{F} has to be included in the momentum balance of Eq. (2.1) to establish the two-way coupling. Equations (2.1) and (2.8) yield a closed system of equations together with the equation of motion

$$\frac{d\mathbf{x}_p}{dt} = \mathbf{v}, \quad (2.9)$$

since the *undisturbed* fluid velocity at the particle position \mathbf{x}_p may be estimated by interpolation of the *disturbed* fluid velocity at the particle position using the Eulerian velocities of the carrier flow for $d_p/\eta_k \ll 1$.

3 Numerical methods

In this chapter, methods for the solution of the system of equations given by Eqs. (2.1), (2.8), and (2.9) will be presented. First, the carrier flow will be discretized using a finite-volume formulation. The discretization yields parameters which will become important in Chapter 4. The formulation of filtered equations for an implicit LES will be presented in Sec. 3.2. This chapter will be closed with the solution schemes for Eqs. (2.8) and (2.9) including a short discussion about the errors introduced by these schemes.

3.1 Spatial and temporal discretization of the carrier flow

The governing equations (2.1) are discretized in time and space using a cell-centered finite-volume formulation. The fluxes are divided into an inviscid part $\bar{\mathbf{H}}_{\text{inv}}$ and a viscous part $\bar{\mathbf{H}}_{\text{visc}}$ as described by Eq. (2.2). The inviscid fluxes are again divided into the convective and the pressure terms and computed by a variant of the AUSM (Liou and Steffen (1993)) of second-order accuracy proposed by Meinke et al. (2002). For the inviscid fluxes, the primitive variables at the cell surfaces are extrapolated according to the MUSCL scheme (Van Leer, 1979), while the extrapolation uses the cell-centered gradients of the primitive variables obtained by a second-order least-squares approach (Schneiders et al., 2016). In order to reduce the dissipative behavior of the second-order discretization in low-Mach number flows, a modified version of the reconstruction method proposed by Thornber et al. (2008), and specified by Hannemann et al. (2012) is used. This reconstruction method alters the extrapolated velocities $u_{L/R}$ at the cell faces which are needed for the AUSM by

$$\begin{aligned} u_L^* &= \frac{u_L + u_R}{2} + z \frac{u_L - u_R}{2}, \\ u_R^* &= \frac{u_L + u_R}{2} + z \frac{u_R - u_L}{2}, \end{aligned} \tag{3.1}$$

where $u_{L/R}^*$ are the altered surface velocities and $z \leq 1$ may be in general an arbitrary function. It will be chosen

$$z = \min(1, \lambda \max(M_r^n, M_l^n)), \quad (3.2)$$

with the normal Mach numbers $M_{r,l}^n$ at the cell surfaces and λ as a grid resolution dependent constant. A value of $z = 1$ recovers the original MUSCL scheme whereas for z tending to zero the surface velocities are obtained by a central differencing such that velocity jumps are smoothed out in low Mach number flows. The viscous fluxes are computed with a low-dissipation variation of the central scheme proposed by Berger et al. (2012), where the normal derivatives of the normal velocity component will be computed at a surface of a cell i with a mixed five- and three-point stencil

$$\left(\frac{\partial u}{\partial x}\right)_{i+1/2} \approx \kappa \frac{u_{i+1} - u_i}{\delta x} + (1 - \kappa) \frac{\left(\frac{\partial u}{\partial x}\right)_i + \left(\frac{\partial u}{\partial x}\right)_{i+1}}{2}, \quad (3.3)$$

where κ is again a grid resolution dependent constant, δx is the grid spacing and x only serves as an auxiliary coordinate direction. All other derivatives are computed via the five-point stencil as proposed by Berger et al. (ibid.). Note, that a value of $\kappa = 0$ yields a low dissipative unstable scheme with a decoupled stencil (ibid.), whereas a value of $\kappa = 1$ results in a common dissipative and stable second-order scheme. The conservative variables \mathbf{Q} in Eq. (2.1) are integrated in time using an explicit five-step Runge-Kutta method (Schneiders et al., 2016).

For implicit LES, such as applied in this thesis, the numerical dissipation serves as a turbulence model (see Sec. 3.2). This dissipation will be controlled by varying the model constants λ and κ . It should be noted that the modified AUSM proposed by Meinke et al. (2002) offers a similar parameter for the pressure flux. However, numerical tests indicate that the pressure fluxes do not play an important role in decaying isotropic turbulence (not shown here).

3.2 Turbulence modeling

In this section, the filtered equations used in LES will be formulated, and the implicit approach will be subsequently compared with the well-known Smagorinsky SGS model (Smagorinsky, 1963). Therefore, the spatial convolution filtering operation is defined as

$$\hat{\phi}(\mathbf{x}, t) = \int_V G(\mathbf{x} - \mathbf{y}, \Delta) \phi(\mathbf{y}, t) d\mathbf{y}, \quad (3.4)$$

where the filter G satisfies the normalization condition

$$\int G(\mathbf{x} - \mathbf{y}, \Delta) d\mathbf{y} = 1, \quad (3.5)$$

$\phi(\mathbf{x}, t)$ is an arbitrary vector, and Δ the filter width. This vector now consists of the large scale part $\hat{\phi}(\mathbf{x}, t)$ and a fine scale part $\phi'(\mathbf{x}, t)$ with

$$\phi(\mathbf{x}, t) = \hat{\phi}(\mathbf{x}, t) + \phi'(\mathbf{x}, t). \quad (3.6)$$

The filtering operation will be applied to the momentum conservation equation in divergence form (2.6). By using the Einstein summation convention, the filtered momentum conservation equation may be written as

$$\frac{\partial \hat{u}_j}{\partial t} + \rho_f \frac{\partial (\hat{u}_i \hat{u}_j)}{\partial x_i} + \frac{\partial \hat{p}}{\partial x_j} = \frac{1}{Re} \frac{\partial \hat{\tau}_{ij}}{\partial x_i} + \frac{\partial \tau_{ij}^R}{\partial x_i}, \quad (3.7)$$

where the filtered solution is given by \hat{u}_j and \hat{p} . Equation (3.7) remains unclosed since the SGS stresses

$$\tau_{ij}^R = \hat{u}_i \hat{u}_j - \widehat{u_i u_j} \neq 0 \quad (3.8)$$

are unknown, unless a suitable model is found. In this context τ_{ij}^R represents the anisotropic part, while the isotropic SGS stresses may be included in the pressure term implicitly. An often used model for SGS stresses is the Smagorinsky SGS model

$$\tau_{ij}^R = 2 (C_S \Delta)^2 \hat{S}_{ij} \left(\sqrt{2 \hat{S}_{ij} \hat{S}_{ij}} \right), \quad (3.9)$$

in which C_S is the Smagorinsky coefficient and the filtered rate-of-strain tensor is stated as

$$\hat{S}_{ij} = \frac{1}{2} \left(\frac{\partial \hat{u}_i}{\partial x_j} + \frac{\partial \hat{u}_j}{\partial x_i} \right). \quad (3.10)$$

Even though it contains the filter width Δ , the filter G is not directly involved but serves merely as a concept. Note, that such an explicit modeling approach works most effectively if the numerical dissipation introduced by numerical schemes for the momentum equations may be neglected. Since this is often not the case, the actual SGS stresses may consist of an explicit modeling component as well as an implicit discretization component (Ghosal, 1996). Meyers et al. (2003) have shown that these different components yield a non-trivial error behavior, where even a finer grid with less dissipation may result in a larger error.

A different perspective of modeling the SGS stresses was given by Boris et al. (1992), who pointed out that monotonicity preserving schemes, i.e. schemes which yield a monotonic solution for any monotonic initial condition and any time step, have a "built-in LES filter and a matched sub-grid model". Schemes, that are

actually developed to capture the entropy satisfying solution of non-linear equations, introduce additional dissipation to ensure stability in the vicinity of shocks which in LES serves as turbulence model. In fact, a modified equation analysis was already performed for several non-oscillatory finite-volume schemes giving a theoretical foundation for this claim (Margolin and Rider, 2007). Additionally, the modified AUSM scheme proposed by Meinke et al. (2002) has been validated thoroughly. However, one heavily relies on the properties of the discretization scheme which leaves considerable uncertainties regarding the accuracy of the predicted flow e.g. in case of mesh refinements. These concerns will be resolved by adjusting the model constants proposed in Sec. 3.1 as will be shown in Chapter 4.

3.3 Solution schemes for the Euler-Lagrange method

Spherical inertial particles are tracked solving the Eqs. (2.8) and (2.9) by a predictor-corrector scheme described by Siewert et al. (2014). In dilute suspensions, such as analyzed in this thesis, particle collisions are statistically irrelevant and thus neglected. In general, particle positions do not coincide with the cell centers and the velocity of the carrier flow "seen" by the particles has to be interpolated. The interpolation is established by a third-order accurate least-squares approach outlined by Siewert (2014). Note, that although a third-order scheme is reported as sufficiently accurate for a DNS (Yeung and Pope, 1988), there is no consensus about the exact formulation of interpolation schemes for particle-laden flow in research (Strutt et al., 2011). However, for LES, filtering effects induced by interpolation schemes appear to be more important. Boivin et al. (1998) analyzed these filtering effects for a fine DNS grid in wave number space and found negligible influence on the results. But these filtering effects happen at a whole range of wave numbers with increasing influence at the highest-resolved wave numbers, which yields a high impact of filtering in LES. Thus, a lower kinetic energy "seen" by particles in LES is expected since the highest-resolved wave numbers in LES may still contain a significant amount of energy.

The coupling force in Eq. (2.8) is established by a projection onto the nearest nine cells weighted by a radial basis function which already has been applied similarly by e.g. Ferrante and Elghobashi (2003), and Boivin et al. (1998). Although this approach is well established for a DNS, little is known about two-way coupling in a LES, since the interaction between particles and carrier flow happens at unresolved scales and may exhibit complex interaction phenomena depending

on the Stokes number (Ferrante and Elghobashi, 2003). As a first attempt for analyzing two-way coupling in LES, the projection approach of the coupling force will be simply adopted. Thus, the interaction between particles and carrier flow happens now at the highest-resolved wave numbers which are grid dependent and do not coincide with the interaction wave numbers of the DNS. It should be noted that several researchers reported accurate results of two-way coupling using a point-force approach of particle-laden LES, as long as τ_p remains larger than the smallest resolved time scales τ_{sgs} (e.g. Boivin et al. (2000), and Urzay et al. (2014)). While the particle dispersion and one-way coupling phenomena may indeed rely only on time scales similar to the particle response time, the reason for these accurate results in two-way coupling LES remains unanswered. In particular, it is doubtful that LES is capable of generating accurate results for particles with diameter $d_p > \eta_k$ while a DNS is restricted to $d_p \ll \eta_k$.

4 Results and discussion

Decaying isotropic turbulence which will serve as the carrier flow for particle-laden flow, will be examined in Sec. 4.1. The flow configuration for this canonical test case will be introduced in Sec. 4.1.1. Afterwards, the model constants proposed in Sec. 3.1 will be determined such that the carrier flow is predicted accurately for several grid widths. The chapter will be closed by Sec. 4.2 with the analysis of particle-laden flow comparing the results of DNS and LES.

4.1 Simulation of the carrier flow

4.1.1 Initial condition and flow configuration

The flow field of a triply periodic cube with an edge length of L is initialized randomly and divergence free while fulfilling the realizability conditions (e.g. Schumann (1977)). The initialization procedure follows the method proposed by Orszag (1969), where a prescribed energy spectrum $E(k)$ serves as initial condition with the model spectrum

$$E(k) = \left(\frac{3u_0^2}{2} \right) \left(\frac{k}{k_p} \right)^2 \exp \left(-\frac{k}{k_p} \right), \quad (4.1)$$

the wave number $k = |\mathbf{k}|$ including the wave number vector \mathbf{k} , the peak wave number k_p , and the initial dimensionless root-mean square velocity (rms-velocity) u_0 . The peak wave number is chosen $k_p = 4k_0$ with $k_0 = 2\pi/L$, whereas u_0 is set to $u_0 = 0.1a$ with the speed of sound a . Thus, neither compressibility effects nor the numerical disturbances for $|\mathbf{u}| \rightarrow 0$ are significant. The pressure field is computed by solving the Poisson equation in spectral space as shown by Schumann and Patterson (1978) and the density field is obtained assuming an isothermal flow field. The initial microscale Reynolds number is set to $Re_{\lambda 0} = u_0 \rho_f \lambda_0 / \mu = 79.1$. Note, that the initial Taylor microscale λ_0 is uniquely defined by the generated initial velocity field, such that the viscosity μ has to be computed from the the initial microscale Reynolds number. The time step size δt was chosen based on the

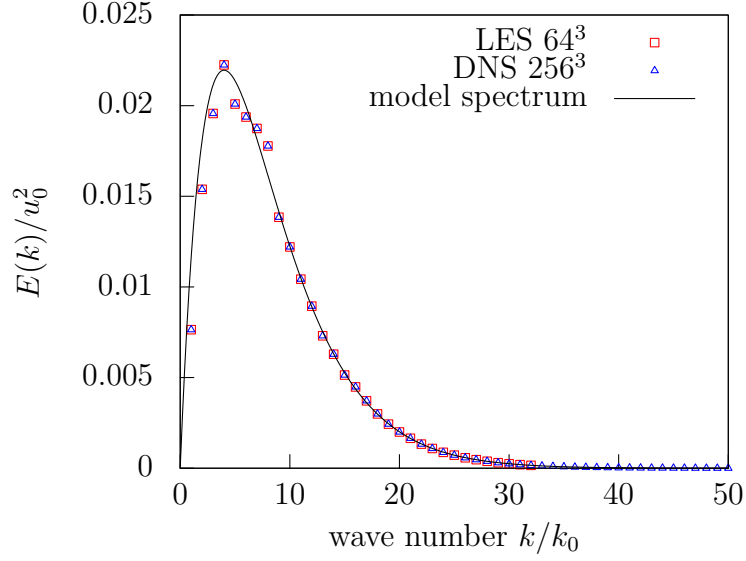


Figure 4.1: Comparison of the initial energy spectrum for a LES and a DNS with the model spectrum for the first 50 wave numbers

CFL-condition with $\delta t = \delta x / (u_0 + a)$ for the DNS and adopted for all LES which yields a lower Courant number for coarser resolutions. However, numerical tests indicate that a lower Courant number has virtually no influence on the statistics. Consequently, it can be assumed that the temporal truncation error, as well as the dissipation introduced by the Runge-Kutta scheme, has only a minor impact on the solution.

This procedure serves as initial condition for the DNS and for the LES, where the maximal resolvable wave number $(k/k_0)_{\max}$ is grid dependent, and thus lower for LES. To ensure comparability between DNS and LES results, the same sequence of random numbers is chosen for the initialization of the velocity field for all simulations. The sequence is cut off at $(k/k_0)_{\max}$ for each simulation, such that the initial energy spectrum of LES and DNS collapses into a single curve for all resolved scales of the LES. Following this procedure, one realization of the initial energy spectrum is shown in Fig. 4.1 for a DNS with 256^3 cells and for a LES with 64^3 cells compared to the model energy spectrum of Eq. (4.1). The maximal resolvable wave number is $(k/k_0)_{\max} = 32$ for the LES and $(k/k_0)_{\max} = 128$ for the DNS. The statistics in wave number space are gained by summing over all wave numbers lying within a shell $|\mathbf{k}| - 1/2 \leq |\mathbf{k}| \leq |\mathbf{k}| + 1/2$. For high wave numbers, a high number of realizations falls into a shell, such that statistical uncertainties are negligible. Thus, the energy spectrum of the discrete realizations for LES and DNS are virtually

congruent with the model spectrum at these wave numbers. Figure 4.1 shows that for wave numbers $(k/k_0) \lesssim 10$, the statistical uncertainties are not negligible. In fact, numerical tests indicate that different sequences of random numbers for the generation of the velocity field lead to different results even in physical space (not shown here). However, the congruence of the LES and DNS results shown in Fig. 4.1 indicates that these deviations are irrelevant for the comparison between LES and DNS. Hence, for all subsequent simulations, the initial energy spectrum shown in Fig. 4.1 will be used as initial condition.

4.1.2 Results

A meaningful comparison between LES and DNS of particle-laden flow requires a sufficient accuracy of the LES of particle-free carrier flow. In this section, the parameters λ for the convective terms and κ for the viscous terms proposed in Sec. 3.1 are configured with the objective to resolve major characteristics of decaying isotropic turbulence accurately by the LES. Two different resolutions for the LES are chosen, namely 64^3 and 128^3 cells, such that the energy containing wave numbers are well resolved, as can be seen in Fig. 4.1. This ensures that the turbulent kinetic energy $E_k = \int_0^\infty E(k)dk = \langle \mathbf{u}'^2/2 \rangle$, where the brackets $\langle \rangle$ denote the spatial ensemble average and \mathbf{u}' the rms-velocity vector, is nearly constant for all resolutions and no filtering operation is necessary for comparison. A lower resolution of the LES (e.g. 32^3 cells) would cut off a significant portion of turbulent kinetic energy and any parameter combination fails to resolve the carrier flow. Figure 4.2a shows an array of curves for the time development of the decay rate of the turbulent kinetic energy dE_k/dt for a fixed $\kappa = 0$ and a variety of values for λ obtained by LES with 64^3 cells. Additionally, the black curve indicates the DNS solution which already has been benchmarked thoroughly by Schneiders et al. (2016). Dimensionless quantities are obtained by multiplying with the initial quantities for the rms-velocity u_0 and for the viscous dissipation rate ϵ_0 of the DNS, and with the edge length L . It can be observed that a growing λ enhances the upwind character of the AUSM and the decay rate of the turbulent kinetic energy. The first time step of the LES shows an overshoot of the decay rate for any parameter combination analyzed in this thesis. However, this overshoot has only minor influence on the subsequent time steps. Indeed, a doubled time step size yields exactly the same statistics, except half of the data points are skipped including the overshoot. Note, that values $\lambda > 1$ would lead to larger values at the cell faces than at the cell centers for high Mach numbers (see Eqs. (3.1) and (3.2)).

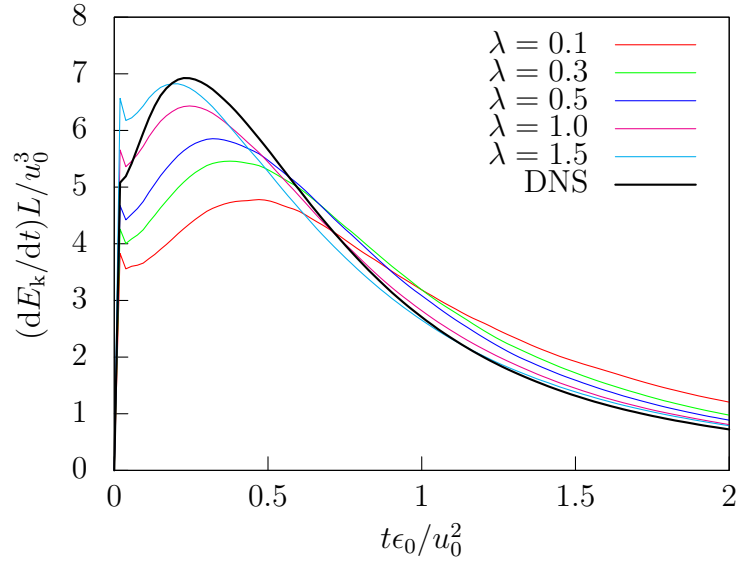
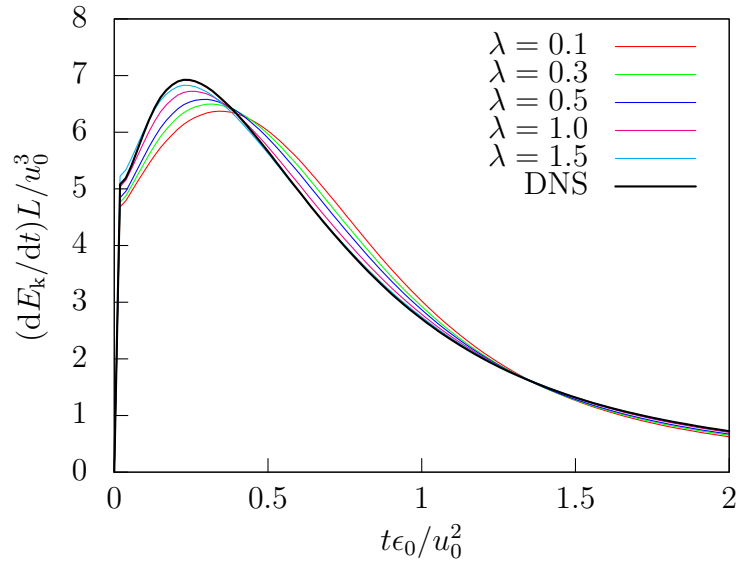
(a) LES with 64^3 cells(b) LES with 128^3 cells

Figure 4.2: Comparison of the decay rate of the turbulent kinetic energy dE_k/dt as a function of time for different parameters λ and fixed $\kappa = 0$ obtained by LES for 64^3 cells and for 128^3 cells with the results of a DNS. A higher λ enhances upwinding and increases the decay rate.

Additionally, any λ fails to predict the decay rate of the turbulent kinetic energy accurately, which leads to the necessity of adjusting the parameter κ for the viscous terms.

Figure 4.2b shows the appropriate statistics for LES with 128^3 cells. Again, an increasing parameter λ enhances the decay rate of the turbulent kinetic energy. As expected, a finer grid resolution reduces the impact of the truncation error, and thus the statistics are already quite similar to the DNS case. The overshoot at the first time step has vanished and even without adjusting the parameter κ accurate results are obtained.

The parameter study for the viscous terms resembles the procedure described above. The parameter for the convective terms is fixed to $\lambda = 1$, which recovers the reconstruction method specified by Hannemann et al. (2012). By varying the parameter κ , one obtains the statistics shown in Figs. 4.3a and 4.3b. Just like before, an increasing parameter κ enhances the decay rate of the turbulent kinetic energy. However, the impact of κ is significantly lower than the impact of λ . Note, that varying the parameters concerning the convective and the viscous terms indeed leads to a different behavior of the statistics, yet an exact analysis of the different impacts would require inhomogeneous flow conditions, which is why this analysis is beyond the scope of this thesis. Since especially for the coarser grid resolution shown in Fig. 4.3a, the statistics still differ from the DNS, a combination of parameters is necessary. Numerical tests have shown that the LES with 64^3 cells, using a combination of parameters $\lambda = 0.6$ and $\kappa = 0.8$, as well as the LES with 128^3 cells, $\lambda = 1.0$, and $\kappa = 0.3$, yields promising results. Hence, these settings will be adopted for all further simulations. The arising statistics are shown in Fig. 4.4. The temporal development of the decay rate of the turbulent kinetic energy (Fig. 4.4a) and consequently the temporal development of the turbulent kinetic energy (Fig. 4.4b) show an excellent agreement with the solution of the DNS. The implicit turbulence model exhibits reliable results. It is therefore assumed, that this setup is suitable to analyze particle-laden decaying isotropic flows with sufficient accuracy. Figure 4.4c shows the skewness S_3 of the velocity derivative comparing the LES for both resolutions with the DNS, defined as

$$S_3 = \frac{\langle (\partial u_i / \partial x_i)^3 \rangle}{\langle (\partial u_i / \partial x_i)^2 \rangle^{3/2}}, \quad (4.2)$$

using the Einstein summation convention. The skewness of the velocity derivative is directly connected to effects concerning the energy cascade including vortex stretching and the transfer of energy between different scales (e.g. Pope (2000)). It

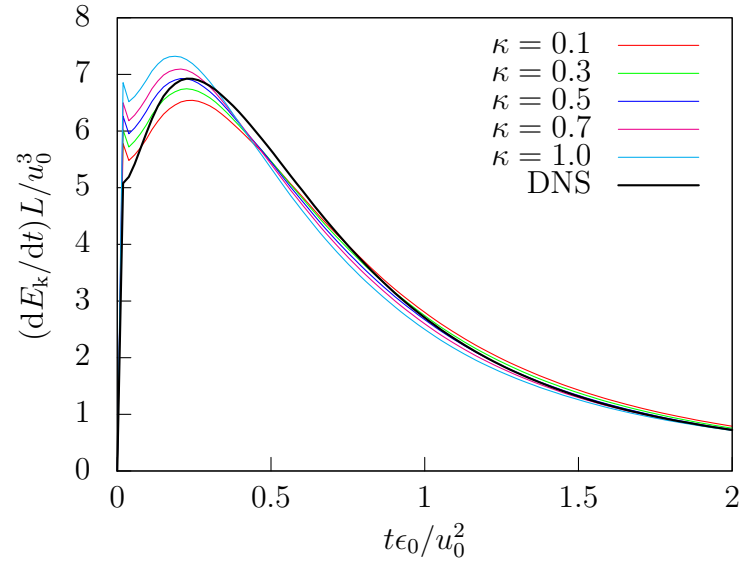
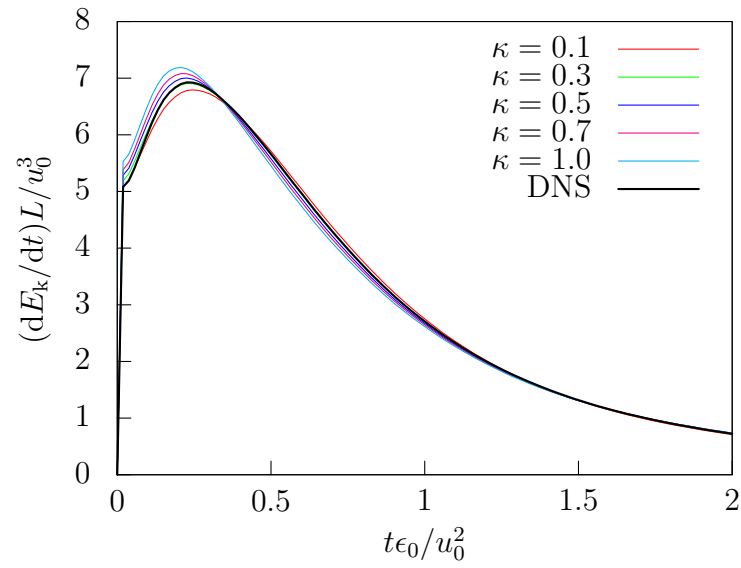
(a) LES with 64^3 cells(b) LES with 128^3 cells

Figure 4.3: Temporal development of the decay rate of the turbulent kinetic energy dE_k/dt for different parameters κ and fixed $\lambda = 1.0$ obtained by LES for 64^3 cells and for 128^3 cells. A higher κ increases the decay rate.

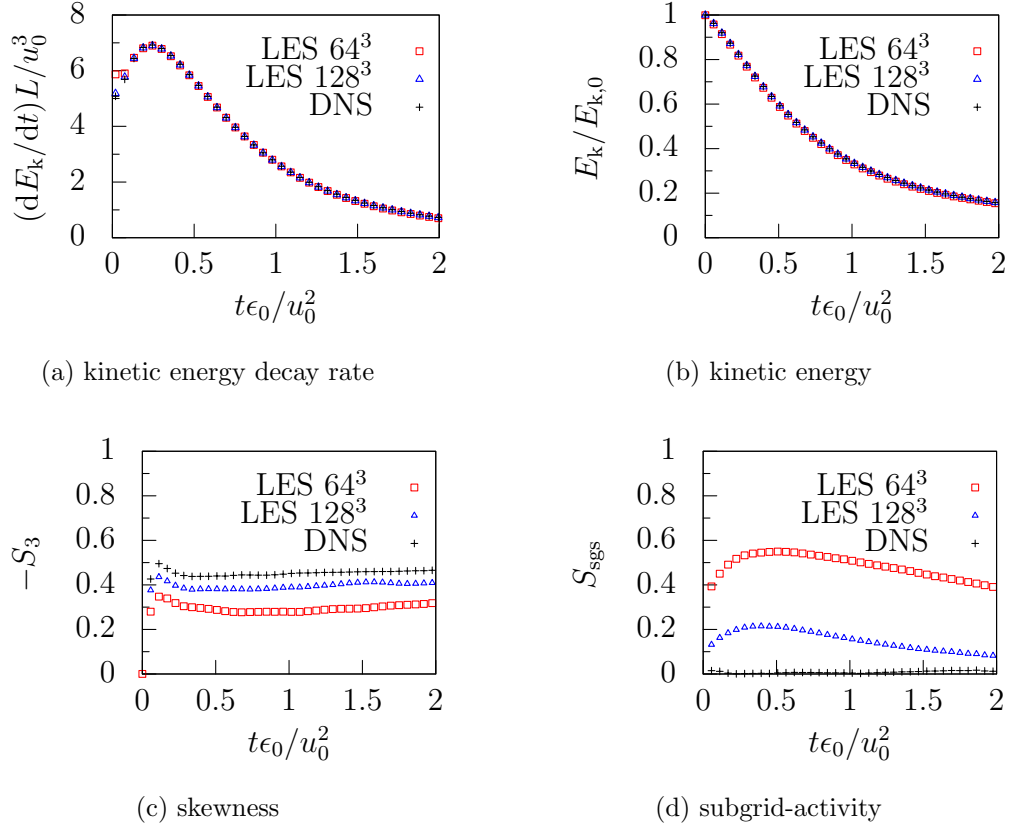


Figure 4.4: Temporal development of the decay rate of the turbulent kinetic energy dE_k/dt (Fig. 4.4a), the turbulent kinetic energy E_k (Fig. 4.4b), the skewness S_3 (Fig. 4.4c) and the subgrid-activity S_{sgs} (Fig. 4.4d). The results of the LES using 64^3 cells with $\lambda = 0.6$ and $\kappa = 0.8$, and the LES using 128^3 cells with $\lambda = 1.0$ and $\kappa = 0.3$ are compared to the results of a DNS.

is therefore a popular indicator for the quality of turbulence models. However, the determination of the exact value is not conclusive. Theoretical analysis predicts a negative constant value for high Reynolds numbers (e.g. Batchelor (1956)), while measurements yield $S_3 \approx -0.4 \pm 0.1$ for the Reynolds number analyzed in this thesis (Van Atta and Antonia, 1980). For LES of decaying isotropic turbulence, it is observed for different turbulence models that the skewness diminishes with decreasing resolution (e.g. Thornber and Drikakis (2006), Geurts et al. (2008)). This behavior may also be recognized in Fig. 4.4c. After a few time steps, the skewness converges to a constant grid dependent level. An accurate prediction of the skewness requires a well-resolved LES and any parameter combination shows a similar or worse behavior. It can be concluded, that the skewness is highly grid resolution dependent and is predicted well compared to other research

findings.

It may become important to quantify how much the turbulence model affects the behavior of the LES. In fact, the parameter studies show less dependency for the resolution of 128^3 than for the resolution of 64^3 cells, as can be observed in Figs. 4.2 and 4.3. For this purpose, the subgrid-activity S_{sgs} introduced by Geurts and Fröhlich (2002) will be adopted, with

$$S_{\text{sgs}} = \frac{dE_k/dt - \epsilon_\nu}{dE_k/dt}, \quad (4.3)$$

where ϵ_ν obtained by $\epsilon_\nu = 2\nu\langle\widehat{S}_{ij}\widehat{S}_{ij}\rangle$ denotes the "resolved" part of the viscous dissipation rate ϵ . The value $S_{\text{sgs}} = 0$ identifies a DNS, where no model for the turbulence is used, whereas $S_{\text{sgs}} = 1$ refers to a LES at infinite Reynolds number, i.e. due to scale separation all viscous effects occur at (unresolved) high wave numbers, and thus have to be modeled. Figure 4.4d shows the subgrid-activity S_{sgs} for the LES using 128^3 and 64^3 cells compared to a DNS. As expected, the subgrid-activity of the DNS remains approximately at 0, whereas a decreasing resolution is connected with an increasing subgrid-activity. Note, that $S_{\text{sgs}} = 1$ is unlikely to be realized for this Reynolds number. Particularly, a flow at a low Reynolds number has no scale separation, i.e. the energy-containing range and the dissipation range might overlap (Batchelor, 1956). Consequently, the resolution of 64^3 appears to be a moderately-resolved LES, while a resolution of 128^3 complies with a well-resolved LES.

Suspended particles are known to interact with a range of wave numbers, which is why the turbulent kinetic energy spectrum of the LES might become important. Figure 4.5 shows the turbulent kinetic energy spectra of two LES using 64^3 cells and 128^3 cells compared with the results of a DNS. As expected, the LES with a resolution of 128^3 cells exhibits accurate results for a broad range of wave numbers. Only at the highest wave numbers, the turbulent kinetic energy accumulates and an overshoot may be observed. The LES with a resolution of 64^3 cells shows good agreement at low wave numbers, moderate deviations at intermediate wave numbers, and also an overshoot at the highest-resolved wave numbers. The overshoots may be well explained by analyzing the discretization of the convective and viscous fluxes, which are controlled by the parameters λ and κ . With decreasing parameters, the numerical convective and viscous fluxes are progressively centralized. Consequently, the numerical damping of high-frequency parts of the solution vanishes, which may be observed as an overshoot at the highest-resolved wave numbers. However, the results are considered acceptable since the interaction with particles may still be analyzed qualitatively in wave number space.

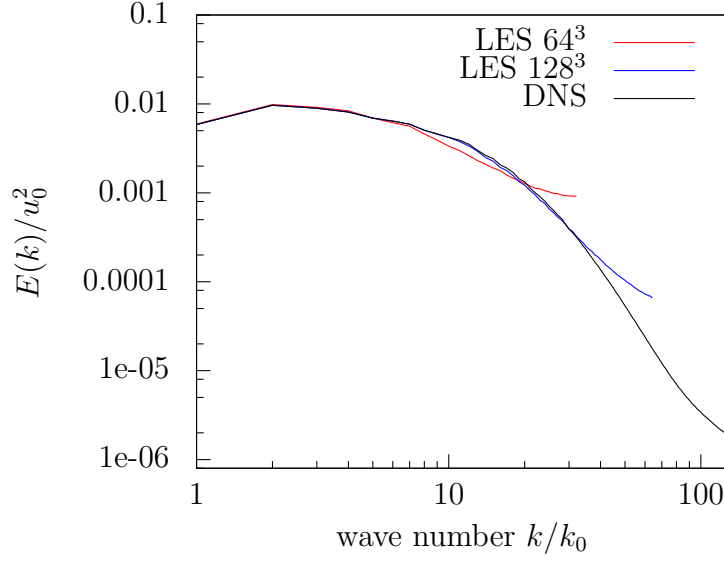


Figure 4.5: Comparison of the energy spectrum for two LES using 64^3 cells and 128^3 cells with a DNS at time $t\epsilon_0/u_0^2 \approx 0.75$.

It can be summarized that the implicit LES of decaying isotropic turbulence shows reliable results compared to a DNS. Major characteristics of the carrier flow are well predicted, such that this setup may be used to analyze particle-laden flow.

4.2 Simulation of particle-laden isotropic decaying turbulence

A cloud of particles is released randomly distributed into the decaying isotropic turbulence described in Sec. 4.1 at $t\epsilon_0/u_0^2 \approx 0.27$ and initialized with the local velocity of the carrier flow. The particle properties are adopted from a case analyzed by Ferrante and Elghobashi (2003), i.e. it is chosen $\Phi_p = 10^{-3}$, $\psi_p = 1$ for $\rho_p/\rho_f = 10^3$, and $d_p/\eta_k = 0.3$ resulting in $St = 5.0$. The reason for these properties is the relatively high Stokes number simultaneously fulfilling the condition $d_p/\eta_k \ll 1$ (see Sec. 2.2). For particles with low Stokes numbers, it is expected that the accuracy of LES without any model is poor, since the interaction occurs at unresolved wave numbers. Therefore, it can be tested whether a model is necessary, even if the particle response time is relatively large. More precisely, Ferrante and Elghobashi (ibid.) have analyzed energy transport terms of particle-laden decaying isotropic

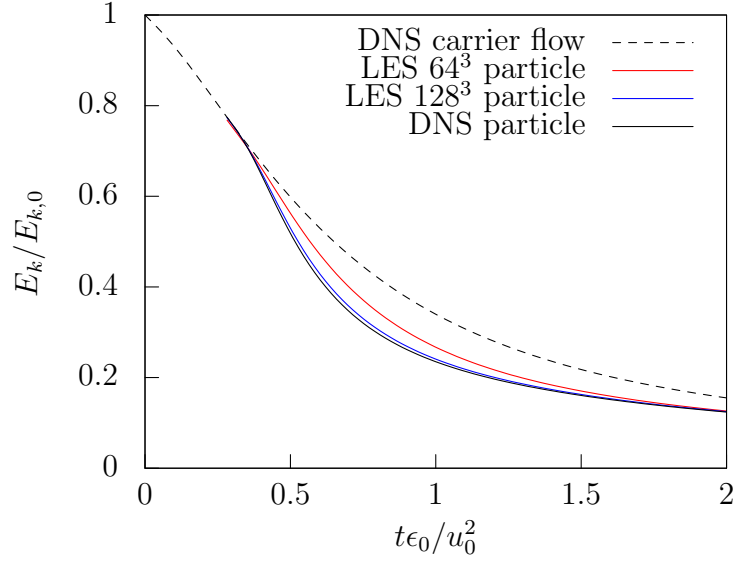


Figure 4.6: Comparison of the turbulent kinetic energy as a function of time for two LES using 64^3 cells and 128^3 cells with a DNS of particle-laden flow. The dashed line is the turbulent kinetic energy of the particle-free carrier flow obtained by a DNS.

turbulent flow in spectral space. They identified three contributions which lead to a temporal change of the spectral kinetic energy: viscous dissipation, triadic energy transportation, and fluid-particle drag interaction. The former two are present in all turbulent flows, whereas the latter is obviously only found in particle-laden flows. Additionally, they observed for the chosen particle properties that the particle drag interaction occurs at wave numbers below $k/k_0 = 32$. Ideally, both resolutions of LES analyzed in this thesis should be capable of resolving the interaction accurately.

Figure 4.6 shows the temporal development of the turbulent kinetic energy normalized by the initial turbulent kinetic energy $E_{k,0}$ for the LES using 64^3 and 128^3 cells, and for the DNS including the particle-free carrier flow. All simulations of particle-laden flow exhibit a reduced turbulent kinetic energy compared to the particle-free carrier flow, which is confirmed by the findings of Ferrante and Elghobashi (2003). The LES using 128^3 cells is in good agreement with the DNS and only minor deviations may be observed, whereas the LES using 64^3 cells shows some discrepancies. Only at the very last time steps, all three statistics converge into a single line. Figure 4.7 shows the decay rate of the turbulent kinetic energy in the same manner as Fig. 4.6. After the injection of the particles, the decay

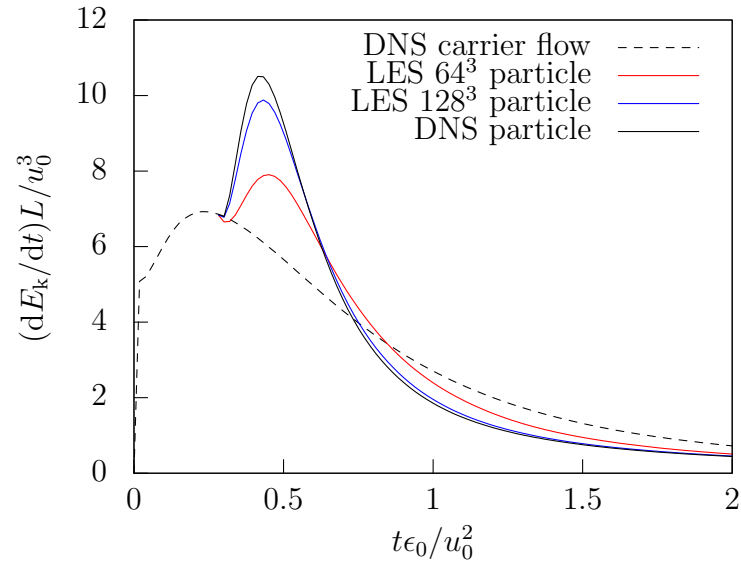


Figure 4.7: Comparison of the decay rate of the turbulent kinetic energy as a function of time for two LES using 64^3 cells and 128^3 cells with a DNS of particle-laden flow. The dashed line is the decay rate of the turbulent kinetic energy of the particle-free carrier flow obtained by a DNS.

rate is underestimated in LES especially for 64^3 cells. Once the turbulent kinetic energy is considerably higher in the LES, which is always connected with a higher decay rate in isotropic decaying turbulence, the curves intersect each other, and the decay rate is overestimated for the LES. Again, the statistics converge into a single line at the last time steps.

Figure 4.8 shows the relative difference between the average kinetic energy of the particles E_p and the turbulent kinetic energy for the three cases. A positive value indicates that the particles have on average less kinetic energy than the surrounding fluid. For DNS and the LES using 128^3 cells, the relative difference exhibits a deflection towards negative values for the first time steps, until it converges to a low, positive constant. Note, that the turbulent kinetic energy "seen" by particles is always lower than the actual turbulent kinetic energy of the carrier flow due to filtering effects introduced by the interpolation scheme (see Sec. 3.3). This underestimation is highly dependent on the grid resolution, since the interpolation occurs at the highest-resolved wave number. Hence, the relative difference for LES using 64^3 cells is shifted significantly towards positive values. This effect is still observable, but may be considered negligible for higher resolutions. In fact, the statistics for the DNS and the LES using 128^3 cells converge to a positive value

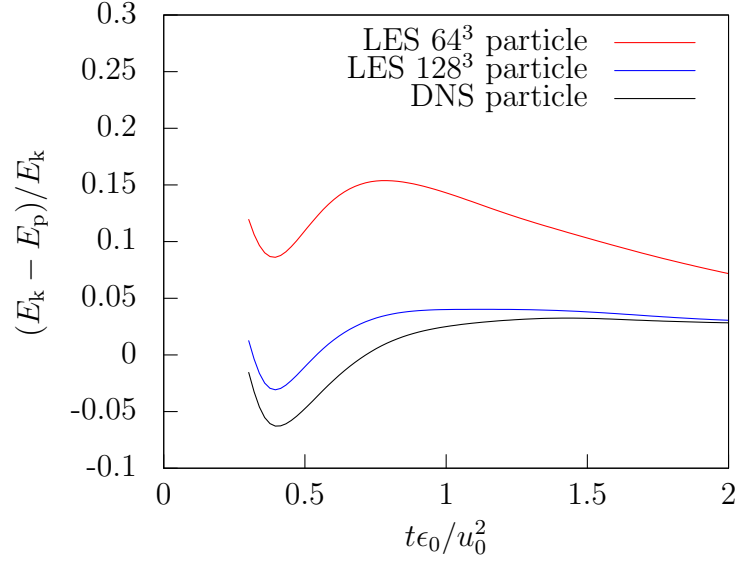


Figure 4.8: Comparison of the relative difference between the kinetic energy of the particles and the turbulent kinetic energy of the particle-laden carrier flow, as a function of time for two LES using 64^3 and 128^3 cells with a DNS.

close to 0 which indicates that preferential concentration is not significant for such high particle response times. The deflection towards negative values at the first time steps may be explained by the high inertia of the particles. At these time steps, the carrier flow experiences a high decay rate and the turbulent kinetic energy quickly decreases (see Fig. 4.7). On the other hand, the particles keep their kinetic energy for a few time steps longer due to their high inertia. For LES using 64^3 cells, the behavior for the first time steps is similar, while in the subsequent time steps the relative difference decreases almost linearly. Figure 4.8 shows that filtering effects due to interpolation certainly have to be reduced by an additional model for particle-laden flow in LES.

The energy spectrum of the particle-laden flow compared to the particle-free carrier flow is shown in Fig. 4.9. Both LES for particle-laden flows show a good agreement for low wave numbers. However, this agreement should be considered with the objection that there are differences in the same range of wave numbers for particle-free LES using 64^3 cells. It is likely, that this agreement stems from two completely different effects, i.e. presence of particles and numerical dissipation, cancelling each other. For the highest-resolved wave numbers, the presence of particles leads to a higher level of energy, which leads certainly to discrepancies between the

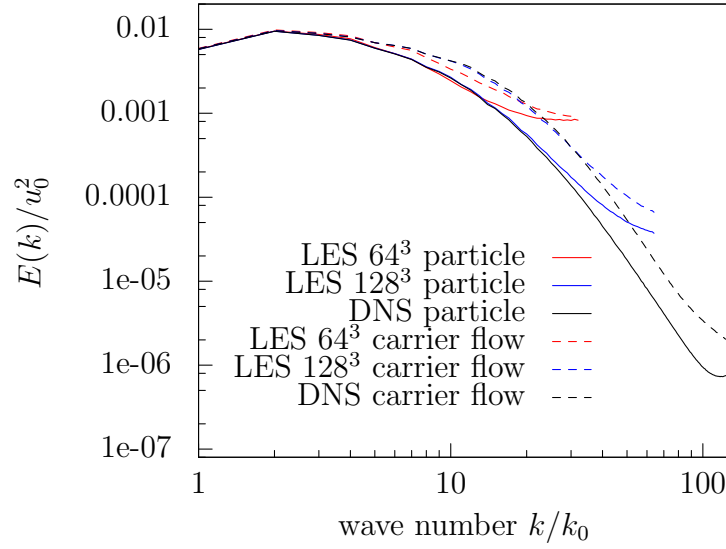


Figure 4.9: Comparison of the energy spectrum for two LES using 64^3 cells and 128^3 cells with a DNS at time $t\epsilon_0/u_0^2 \approx 0.75$. The dashed lines represent the particle-free carrier flow shown in Fig. 4.5.

different resolutions. The question arises, which contributions are responsible for the discrepancies in spectral space. Especially the viscous dissipation, the triadic energy transportation and the fluid-particle drag interaction have to be identified for further analysis, which will be left for future investigations.

5 Conclusion and outlook

Implicit LES has been performed for particle-laden decaying isotropic turbulence including two-way coupling effects. Therefore, the numerical fluxes of the convective and the viscous terms have been enhanced by parameters, which allow to control the numerical dissipation. Subsequently, the parameters have been benchmarked using the case of particle-free decaying isotropic turbulence for two resolutions, namely 64^3 and 128^3 cells, such that the solution of the LES is in good agreement with the results of a DNS. In particular, the LES is able to reproduce the results of a DNS accurately concerning the turbulent kinetic energy as a function of time, while the skewness corresponds to similar studies. The energy spectrum matches well for the energy-containing large scales. Only the highest-resolved wave numbers show an overshoot due to the reduced damping of the highest frequencies by the increased centralizing of the numerical scheme. The excellent results of the implicit LES of particle-free flow permit to proceed with particle-laden flows. A cloud of heavy particles has been randomly distributed in the domain and its temporal behavior has been investigated. Two-way coupling effects influence the turbulent kinetic energy as well as the energy spectrum of the carrier flow significantly compared to the particle-free case. As a first step, the two-way coupling mechanism for LES has been adopted from the DNS, i.e. no additional model has been introduced for the interaction. DNS and LES of particle-laden flows share most of the characteristics with increasing differences for decreasing resolution. The turbulent kinetic energy of the carrier flow is overestimated for the LES using 64^3 cells, whereby LES, as well as DNS, show a decreased turbulent kinetic energy compared to the particle-free carrier flow. Some analysis has been performed to identify the reason for the deviations of the coarser LES. A comparison of the relative difference between the kinetic energy of the particles and the turbulent kinetic energy of the carrier flow indicates that the interpolation of fluid velocities onto the actual particle position introduces grid dependent filtering effects. Especially the particles in the LES using 64^3 cells experience a significantly slower flow. The energy spectrum of the particle-laden carrier flow shows that the LES is in good agreement with the results of the DNS at low wave numbers. However, all spectra show an accumulation

of kinetic energy at the highest-resolved wave number, and therefore significant discrepancies arise between the different resolutions.

The setup introduced in this thesis may now be used for further analysis of models for particle-laden flows in LES. More information is required to understand the fluid-particle interaction in wave number space. Particularly, the range of the drag force in the wave number space of the LES compared to the DNS has to be identified, giving some insight whether the projection of the drag force onto the grid performs well. Furthermore, recent developments for models concerning the dispersion of particles (one-way coupling) show promising results. Especially the approximate deconvolution method (ADM) which tries to approximate the unresolved parts of the velocity field (Stolz and Adams, 1999) appears to be promising for modeling particle-laden flows in LES (see e.g. Shotorban and Mashayek (2005)). More recently, access has been gained to fully-resolved DNS of particle-laden flows, which does not rely on the Euler-Lagrange method (Schneiders et al., 2016). Hence, the possibility arises to generate reference data for LES which does not restrict the particle diameter to $d_p \ll \eta_k$. In the long-term, this allows the development of LES models for the important case $d_p > \eta_k$ relating to industrial and environmental flows.

Bibliography

- Apte, S. V., K. Mahesh, P. Moin, and J. C. Oefelein. “Large-eddy simulation of swirling particle-laden flows in a coaxial-jet combustor”. In: *Int. J. Multiph. Flow* 29 (2003), pp. 1311–1331.
- Armenio, V., U. Piomelli, and V. Fiorotro. “Effect of the subgrid scales on particle motion”. In: *Phys. Fluids* 11 (1999), pp. 3030–3042.
- Balachandar, S. and J. K. Eaton. “Turbulent Dispersed Multiphase Flow”. In: *Annu. Rev. Fluid. Mech.* 42 (2010), pp. 111–133.
- Batchelor, G. K. *The theory of homogeneous turbulence*. Cambridge University Press, 1956. Chap. 6.4, pp. 114–121.
- Berger, M., M. J. Aftosmis, and S. R. Allmaras. “Progress Towards a Cartesian Cut-Cell Method for Viscous Compressible Flow”. In: 50th AIAA Aerospace Sciences Meeting Including the New Horizons Forum and Aerospace Exposition. 2012.
- Bermudez, A., J. L. Ferin, A. Linan, and L. Saavedra. “Numerical simulation of group combustion of pulverized coal”. In: *Combust. Flame* 158 (2011), pp. 1852–1865.
- Boivin, M., O. Simonin, and K. D. Squires. “Direct numerical simulation of turbulence modulation by particles in isotropic turbulence”. In: *J. Fluid Mech.* 375 (1998), pp. 235–263.
- Boivin, M., O. Simonin, and K. D. Squires. “On the prediction of gas-solid flows with two-way coupling using large eddy simulation”. In: *Phys. Fluids* 12 (2000), pp. 2080–2090.
- Boris, J. P., F. F. Grinstein, E. S. Oran, and R. L. Kolbe. “New insights into large eddy simulation”. In: *Fluid. Dyn. Res.* 10 (1992), pp. 199–228.
- Elghobashi, S. and G. C. Truesdell. “Direct simulation of particle dispersion in a decaying isotropic turbulence”. In: *J. Fluid Mech.* 242 (1992), pp. 655–700.
- Elghobashi, S. and G. C. Truesdell. “On the two-way interaction between homogeneous turbulence and dispersed solid particles. I: Turbulence modification”. In: *Phys. Fluids A* 5 (1993), pp. 1790–1801.

- Ferrante, A. and S. Elghobashi. “On the physical mechanisms of two-way coupling in particle-laden isotropic turbulence”. In: *Phys. Fluids* 15 (2003), pp. 315–329.
- Franchetti, B. M., F. C. Marincola, S. Navarro-Martinez, and A. M. Kempf. “Large Eddy simulation of a pulverised coal jet flame”. In: *Proc. Combust. Inst.* 34 (2013), pp. 2419–2426.
- Geurts, B. J. and J. Fröhlich. “A framework for predicting accuracy limitations in large-eddy simulation”. In: *Phys. Fluids* 14 (2002), pp. L41–L44.
- Geurts, B. J., A. K. Kuczaj, and E. S. Titi. “Regularization modeling for large-eddy simulation of homogeneous isotropic decaying turbulence”. In: *J. of Phys. A: Math. Theor.* 41 (2008), p. 344008.
- Ghosal, S. “An Analysis of Numerical Errors in Large-Eddy Simulations of Turbulence”. In: *J. Comp. Phys.* 125 (1996), pp. 187–206.
- Gobert, C. and M. Manhart. *A priori and a posteriori analysis of models for Large-Eddy simulation of particle-laden flow*. 2010. arXiv: 1004.5598v1.
- Hannemann, V., A. Siegmund, K. Oßwald, P. Birken, K. Weinman, and A. Meister. “Dissipation of upwind schemes at high wave numbers”. In: Seventh International Conference on Computational Fluid Dynamics. 2012.
- Liou, M.-S. and C. J. Steffen. “A New Flux Splitting Scheme”. In: *J. Comp. Phys.* 107 (1993), pp. 23–39.
- Margolin, L. G. and W. J. Rider. *Implicit Large Eddy Simulation*. Computing Turbulent Fluid Dynamics. Cambridge University Press, 2007, pp. 195–221.
- Maxey, M. R. and J. J. Riley. “Equation of motion for a small rigid sphere in a nonuniform flow”. In: *Phys. Fluids* 26 (1983), pp. 883–889.
- Meinke, M., W. Schröder, E. Krause, and T. Rister. “A comparison of second- and sixth-order methods for large-eddy simulations”. In: *Comput. Fluids* 31 (2002), pp. 695–728.
- Meyers, J., B. J. Geurts, and M. Baelmans. “Database analysis of errors in large-eddy simulation”. In: *Phys. Fluids* 15 (2003), pp. 2740–2755.
- Orszag, S. A. “Numerical Methods for the Simulation of Turbulence”. In: *Phys. Fluids* 12 (1969), pp. 250–257.
- Pope, S. B. *Turbulent Flows*. Cambridge University Press, 2000, pp. 183–186.
- Schneiders, L., C. Günther, M. Meinke, and W. Schröder. “An efficient conservative cut-cell method for rigid bodies interacting with viscous compressible flows”. In: *J. Comp. Phys.* 311 (2016), pp. 62–86.
- Schumann, U. “Realizability of Reynolds-stress turbulence models”. In: *Phys. Fluids* 20 (1977), pp. 721–725.

- Schumann, U. and G. S. Patterson. “Numerical study of pressure and velocity fluctuations in nearly isotropic turbulence”. In: *J. Fluid Mech.* 88 (1978), pp. 685–709.
- Shotorban, B. and F. Mashayek. “Modeling subgrid-scale effects on particles by approximate deconvolution”. In: *Phys. Fluids* 17 (2005), p. 081701.
- Siewert, C., R. P. J. Kunnen, M. Meinke, and W. Schröder. “Orientation statistics and settling velocity of ellipsoids in decaying turbulence”. In: *Atmos. Res.* 142 (2014), pp. 45–56.
- Siewert, C. “Numerical Analysis of Particle Collisions in Isotropic Turbulence”. PhD thesis. RWTH Aachen, 2014, pp. 25–27.
- Smagorinsky, J. “General circulation experiments with the primitive equations: I. The basic equations”. In: *Mon. Weather Rev.* 91 (1963), pp. 99–164.
- Squires, K. D. and J. K. Eaton. “Preferential concentration of particles by turbulence”. In: *Phys. Fluids A* 3 (1991), pp. 1169–1178.
- Stolz, S. and N. A. Adams. “An approximate deconvolution procedure for large-eddy simulation”. In: *Phys. Fluids* 11 (1999), pp. 1699–1701.
- Strutt, H. C., S. W. Tullis, and M. F. Lightstone. “Numerical methods for particle-laden DNS of homogeneous isotropic turbulence”. In: *Comput. Fluids* 40 (2011), pp. 210–220.
- Thorner, B. and D. Drikakis. “Large-eddy simulation of isotropic homogeneous decaying turbulence”. In: European Congress on Computational Methods in Applied Sciences and Engineering CFD. 2006.
- Thorner, B., A. Mosedale, D. Drikakis, D. Youngs, and R. J. R. Williams. “An improved reconstruction method for compressible flows with low Mach number features”. In: *J. Comp. Phys.* 227 (2008), pp. 4873–4894.
- Urzay, J., M. Bassenne, G. I. Park, and P. Moin. “Characteristic regimes of subgrid-scale coupling in LES of particle-laden turbulent flows”. In: *CTR Annu. Res. Briefs.* 2014.
- Van Atta, C. W. and R. A. Antonia. “Reynolds number dependence of skewness and flatness factors of turbulent velocity derivatives”. In: *Phys. Fluids* 23 (1980), pp. 252–257.
- Van Leer, B. “Towards the ultimate conservative difference scheme V. A second-order sequel to Godunov’s method”. In: *J. Comp. Phys.* 32 (1979), pp. 101–136.
- Wang, L.-P. and M. R. Maxey. “Settling velocity and concentration distribution of heavy particles in homogeneous isotropic turbulence”. In: *J. Fluid Mech.* 256 (1993), pp. 27–68.

-
- Yeung, P. K. and S. B. Pope. “An Algorithm for Tracking Fluid Particles in Numerical Simulations of Homogeneous Turbulence”. In: *J. Comp. Phys.* 79 (1988), pp. 373–416.